

Supporting Information

Improving built-in electric fields for effective photocatalytic activity in rationally designed electron transfer pathway of TiO₂@MoS₂/Bi₂S₃

Jianyu Gong ^{a, b, *}, Yihang Zhang ^{a, b}, Ting Yue ^{a, b}, Yao Lu ^{a, b}

^a School of Environmental Science & Engineering,

Huazhong University of Science and Technology (HUST),

1037 Luoyu Road, Wuhan, Hubei, 430074, China

^b Hubei Key Laboratory of Multi-media Pollution Cooperative Control in Yangtze

Basin,

School of Environmental Science & Engineering,

Huazhong University of Science and Technology (HUST),

1037 Luoyu Road, Wuhan, Hubei, 430074, China

* Corresponding author contact information:

Professor Jianyu Gong

E-mail address: jygong@hust.edu.cn

This Supporting Information Contains the Following Sections:

Table S1. Reagent dosage in the synthesis of $\text{TiO}_2@\text{MoS}_2$

Fig. S1 XRD of $\text{TiO}_2@\text{MoS}_2$ with different Ti: Mo molar ratios and TiO_2

Fig. S2 TEM, and HRTEM of $\text{TiO}_2@\text{MoS}_2$ and $\text{TiO}_2@\text{MoS}_2/\text{Bi}_2\text{S}_3$

Fig. S3 High-angle annular dark-field scanning transmission electron microscopy

(HAADF-STEM) with energy dispersive X-ray spectra of $\text{TiO}_2@\text{MoS}_2/\text{Bi}_2\text{S}_3$

Fig. S4 XPS peak position spectra of $\text{TiO}_2@\text{MoS}_2$ -125, $\text{TiO}_2@\text{MoS}_2/\text{Bi}_2\text{S}_3$ -7 and the used $\text{TiO}_2@\text{MoS}_2/\text{Bi}_2\text{S}_3$ -7 samples: (A) global energy survey, (B) C1s, (C) Ti2p, (D) O1s, (E) Mo3d, (F) S2p and (G) Bi4f.

Fig. S5 (A) $\ln(C/C_0)$ vs reaction time and (B) rate constant of $\text{TiO}_2@\text{MoS}_2$ composite with different molar ratios curve and TiO_2

Fig. S6 (A) $\ln(C/C_0)$ vs reaction time and (B) rate constant of $\text{TiO}_2@\text{MoS}_2/\text{Bi}_2\text{S}_3$ composite with different Bi_2S_3 spin coating times.

Fig. S7 SEM of recycling $\text{TiO}_2@\text{MoS}_2/\text{Bi}_2\text{S}_3$ -7 composites for five runs

Fig. S8 EDS mapping of recycling $\text{TiO}_2@\text{MoS}_2/\text{Bi}_2\text{S}_3$ -7 composites and the corresponding EDS spectrum for 5th used $\text{TiO}_2@\text{MoS}_2/\text{Bi}_2\text{S}_3$ -7

Fig. S9 XRD pattern of recycling $\text{TiO}_2@\text{MoS}_2/\text{Bi}_2\text{S}_3$ -7 compared with standard PDF card after stability test

Fig. S10 High-angle annular dark-field scanning transmission electron microscopy (HAADF-STEM) of recycling $\text{TiO}_2@\text{MoS}_2/\text{Bi}_2\text{S}_3$

Fig. S11 High-angle annular dark-field scanning transmission electron microscopy (HAADF-STEM) with energy dispersive X-ray spectra of recycling $\text{TiO}_2@\text{MoS}_2/\text{Bi}_2\text{S}_3$

Fig. S12 UV-vis absorption spectra of (A) $\text{TiO}_2@\text{MoS}_2$ with different molar ratios. (B) $\text{TiO}_2@\text{MoS}_2/\text{Bi}_2\text{S}_3$ with different spin coating times.

Fig. S13 Kubelka–Munk function VS the energy of incident light plots of (A) $\text{TiO}_2@\text{MoS}_2$ with different molar ratios. (B) $\text{TiO}_2@\text{MoS}_2/\text{Bi}_2\text{S}_3$ with different spin coating times.

Fig. S14 Energy band gap of TiO_2 , $\text{TiO}_2@\text{MoS}_2$ and $\text{TiO}_2@\text{MoS}_2/\text{Bi}_2\text{S}_3$

Fig. S15 Linear Sweep Voltammetry (LSV) curves of TiO_2 , $\text{TiO}_2@\text{MoS}_2$ and $\text{TiO}_2@\text{MoS}_2/\text{Bi}_2\text{S}_3$ under visible-light illumination

Fig. S16 Electrochemical Impedance Spectroscopy (EIS) of (A) $\text{TiO}_2@\text{MoS}_2$ with different Mo doping proportions and (B) $\text{TiO}_2@\text{MoS}_2/\text{Bi}_2\text{S}_3$ with various Bi_2S_3 spin coating times at applied potential of 0.5 V

Fig. S17 Cyclic Voltammogram (CV) for (A) TiO_2 , (B) $\text{TiO}_2@\text{MoS}_2$ (C) and $\text{TiO}_2@\text{MoS}_2/\text{Bi}_2\text{S}_3$ in the region of $0.20 \sim 0.30$ V vs. RHE with various scans

Fig. S18 Current density differences plotted against scan rates of TiO_2 , $\text{TiO}_2@\text{MoS}_2$ and $\text{TiO}_2@\text{MoS}_2/\text{Bi}_2\text{S}_3$

Fig. S19 Mott–Schottky (M–S) plots of (A) TiO_2 , (B) MoS_2 and (C) Bi_2S_3 separately

Fig. S20 (A) Fluorescence spectra of 7-hydroxycoumarin (7-HOC) in 0.1 mM coumarin solution and (B) $\cdot\text{OH}$ generation amount in the presence of various as-synthesized samples after 10 min visible-light illumination. (C) UV-Vis absorption spectra of NBT (2.5×10^{-2} mM) and (D) $\text{O}_2^{\cdot-}$ generation amount on different as-synthesized samples after 10 min visible-light illumination.

Experiment procedures

1. Materials

Absolute ethanol (A.R., $\geq 99.7\%$), TBOT ($C_{16}H_{36}O_4Ti$, C.P., $\geq 98.0\%$), sulfourea (CH_4N_2S , A.R.), sodium sulfide (Na_2S , A.R.), sodium molybdate ($Na_2MoO_4 \cdot 2H_2O$, A.R.), tetrachlorophenol (C_6H_5ClO , A.R.), $Bi(NO_3)_3 \cdot 5H_2O$ (A.R., 99.9%) were all obtained from Sinopharm Chemical Regent Co., Ltd. (Shanghai, China). The ultrapure water with a resistance of $18.2 M\Omega \text{ cm}$ were used in whole experiment.

2. Material Characterization

The crystal structure of the samples was examined by X-ray spectroscopy (XRD, 2θ ranges from 10° to 80° , using a diffractometer at 40 kV and 40 mA). The morphology and element distribution were characterized by transmission electron microscopy (TEM, JEM-2100F electron microscope operating at 200 kV), elemental mapping. The chemical compositions were analyzed by X-ray photoelectron spectroscopy (XPS, conducted on a 5300 ESCA instrument (Perkin-Elmer PHI Co., USA) using an Al $K\alpha$ X-ray source at a power of 250 W). The UV-Vis diffuse reflection spectra (UV-Vis DRS) was obtained by the Scan UV-Vis spectrophotometer (UV-2600, Shimadzu) with 100% $BaSO_4$ as a reference. The photoluminescence (PL) spectra were acquired using an Edinburgh Analytical Instrument (FLS1000) at room temperature with a xenon lamp as the excitation source at the excitation wavelength of 325 nm of as-prepared catalyst. Time-resolved PL spectra were determined on a HORIBA Delta Pro under 325 nm excitation. The pump laser of 325 nm light was generated by a Q-switched Nd: YAG laser system using a third harmonic process on its fundamental output. The signal was

collected by a monochromator and then recorded by a sensitive photomultiplier and traced by a TDS 3012C digital signal analyzer. Time-resolved PL experiment was carried out in air-saturated aqueous solutions. At the sample position, the average power were around 80 mW for the pump beam. Time resolved fluorescence decay traces were deconvoluted from the signal and fitted using the FluoFit 4.4 package (Picoquant GmbH). The experimental decay traces were fitted to multi-exponential functions via a Levenberg-Marquardt algorithm-based nonlinear least-squares error minimization deconvolution method. Usually, up to four different exponential terms were used to fit the experimental decay traces. The quality of the fits was judged by the reduced chi-squared method, the weighted residuals and the correlation functions. The latter two were checked for random distributions. Subsequently, the average photoluminescence lifetime was calculated by the following equation

$$\tau_{\text{ave}} = \sum A_i \tau_i^2 / \sum A_i \tau_i$$

Where A_i are the pre-exponential factors and τ_i are the lifetimes obtained in the multiexponential fitting of the decay kinetics.

A solar cell quantum efficiency (QE)/IPCE measurement system (CEL-QPCE3000) was applied to measure IPCE. The surface potential was monitored by KPFM in dark using AFM system (SPA-300HV) equipped with a SKPM module. Surface Photovoltage (SPV) spectroscopy measurement system is constituted of a source of monochromatic light, a lock-in amplifier (SR830-DSP) with a light chopper (SR540), a photovoltaic cell, and a computer. Electron spin resonance (ESR) spectra were obtained with a Bruker EPR A300 spectrometer at room temperature under visible

light ($\lambda > 420\text{nm}$). The detection method of DMPO- $\cdot\text{OH}$ and DMPO- $\cdot\text{O}_2^-$ was as follows: 5 mg sample was dissolved in 5 mL solvent, 56 μL DMPO was mixed with the solvent, the solvent for detecting OH was water, and the solvent for detecting $\cdot\text{O}_2^-$ was methanol. Singlet oxygen ($^1\text{O}_2$) was measured by dispersing 5 mg samples in 150 mmol/L TEMP solution prepared with water as solvent, and then taking the mixture for 10 min and 15 min respectively under visible light irradiation for in-situ test. Furthermore, generation concentration of ROS by as-synthesized photocatalysts under visible-light irradiation was measured, and relevant calculation methods and process was described in quantitation experiments of $\cdot\text{OH}$ and $\cdot\text{O}_2^-$ section, also in SI file. Then concentration of 7-HOC was detected by fluorescence spectrometer (Hitachi-7100 JPN). The excitation wavelength (WL) was set as 344 nm, the emission starting WL was 440 nm, the emission end WL was 480 nm and the slit width was 2.5 nm. The concentration of NBT was measured at 200-500 nm by UV-Vis Spectrophotometer (UV-2600 JPN).

3. Photoelectrochemical (PEC) Characterization

The PEC characterizations were conducted by an electrochemical workstation (CHI660E) using a conventional three electrode system, in which conductive glass coated with photocatalytic materials was used as the working electrode, Pt electrode was used as the counter electrode, saturated Ag/AgCl electrode was used as the reference electrode, and 0.1 mol/L Na_2SO_4 solution was used as the electrolyte solution. The frequency range and AC amplitude of EIS were set as 0.01 to 1×10^5 Hz and 0.5 V, respectively. Mott-Schottky plots were examined with a scan rate of 5 mV/s at 1000

Hz. Fabrication procedures of preparing working electrode as follows: 2 mg of photocatalyst powders were dispersed in mixed solution containing 800 μ L of deionized water, 150 μ L of ethanol and 50 μ L of Nafion with ultrasound treatment for 30 min. Then the mixed solution was dropped and dried several times on FTO substrate ($1 \times 1 \text{ cm}^2$). In addition, the light source of photocurrent response was supplied by a 300W Xe lamp, whole operation should be conducted under visible light (>420nm) irradiation, and the photocurrent density is measured during five light-on and light-off cycles operation, turning on and off the light source every 20 seconds. All the collected potential versus Ag/AgCl ($E_{\text{Ag/AgCl}}$) values were converted to normal hydrogen electrode (NHE) potential (E_{NHE}) by the formula $E_{\text{NHE}} = E_{\text{Ag/AgCl}} + 0.197$.

4. DFT Calculations

Calculations based on first-principles density functional theory (DFT) were executed utilizing the Vienna Ab initio Simulation Package (VASP)^[S1] in conjunction with the Projector Augmented Wave (PAW) methodology.^[S2] The exchange-correlation functional was managed within the parameters of the Generalized Gradient Approximation (GGA), adopting the Perdew-Burke-Ernzerhof (PBE) functional.^[S3] The energy cutoff set at 500 eV, and the geometric relaxation was carried through until the forces acting on each atom were less than 0.03 eV/ \AA . The K-points is performed at the Gamma point. And, the energy convergence threshold was less than 10^{-5} eV. A vacuum layer of 15 \AA is added perpendicular to the sheet to avoid artificial interaction between periodic images. The Brillouin zone integration is performed using a 3x4x1 k-mesh. For the TiO₂ surface geometry optimization, the structure are relaxed, while for

the heterostructure surface geometry optimization, only the TiO₂ structure are fixed.

Table. S1 Reagent dosage in the synthesis of $\text{TiO}_2@\text{MoS}_2$

Sample	TiO_2/g	Na_2MoO_4 solution/mL	Thiourea solution / mL	nMo: nTi
$\text{TiO}_2@\text{MoS}_2-50$	0.16	4.000	6.000	1:50
$\text{TiO}_2@\text{MoS}_2-75$	0.16	2.667	7.333	1:75
$\text{TiO}_2@\text{MoS}_2-100$	0.16	2.000	8.000	1:100
$\text{TiO}_2@\text{MoS}_2-125$	0.16	1.600	8.400	1:125
$\text{TiO}_2@\text{MoS}_2-150$	0.16	1.000	9.000	1:150

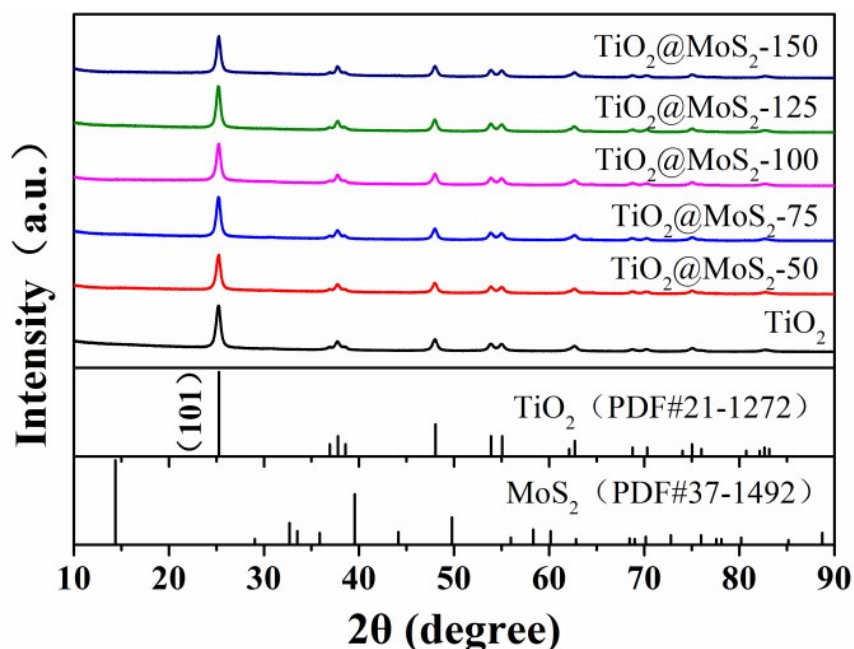


Fig. S1 XRD of $\text{TiO}_2@\text{MoS}_2$ with different Ti: Mo molar ratios and TiO_2

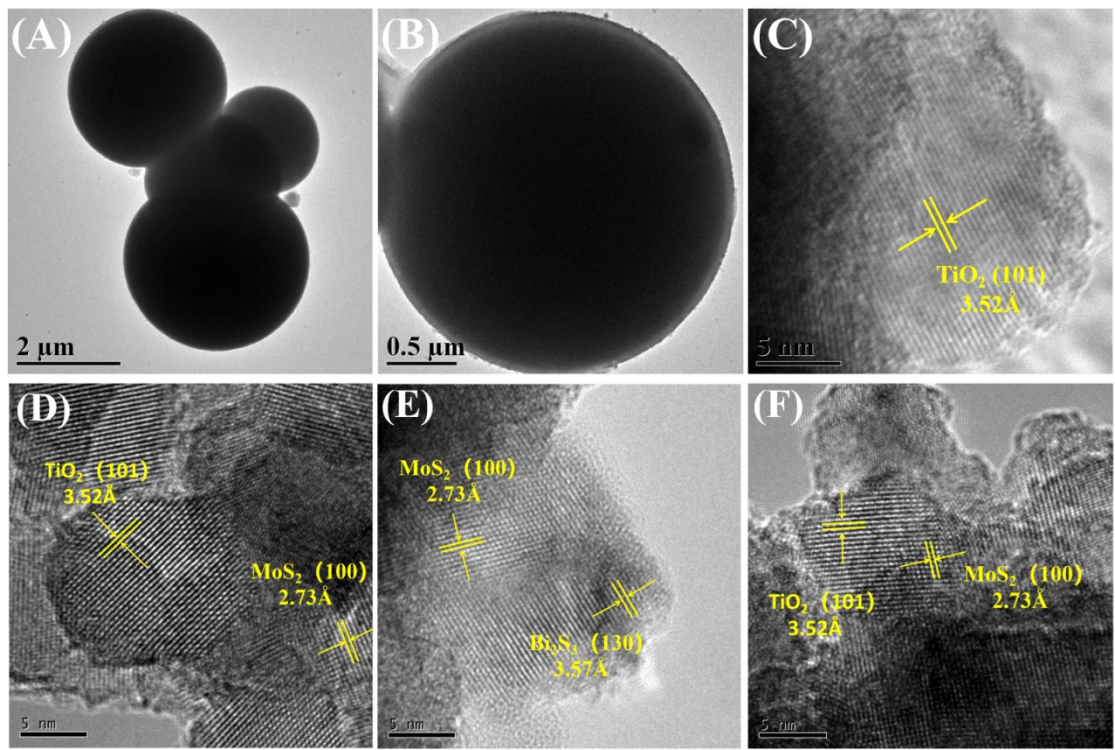


Fig. S2 TEM, and HRTEM of $\text{TiO}_2@\text{MoS}_2$ and $\text{TiO}_2@\text{MoS}_2/\text{Bi}_2\text{S}_3$

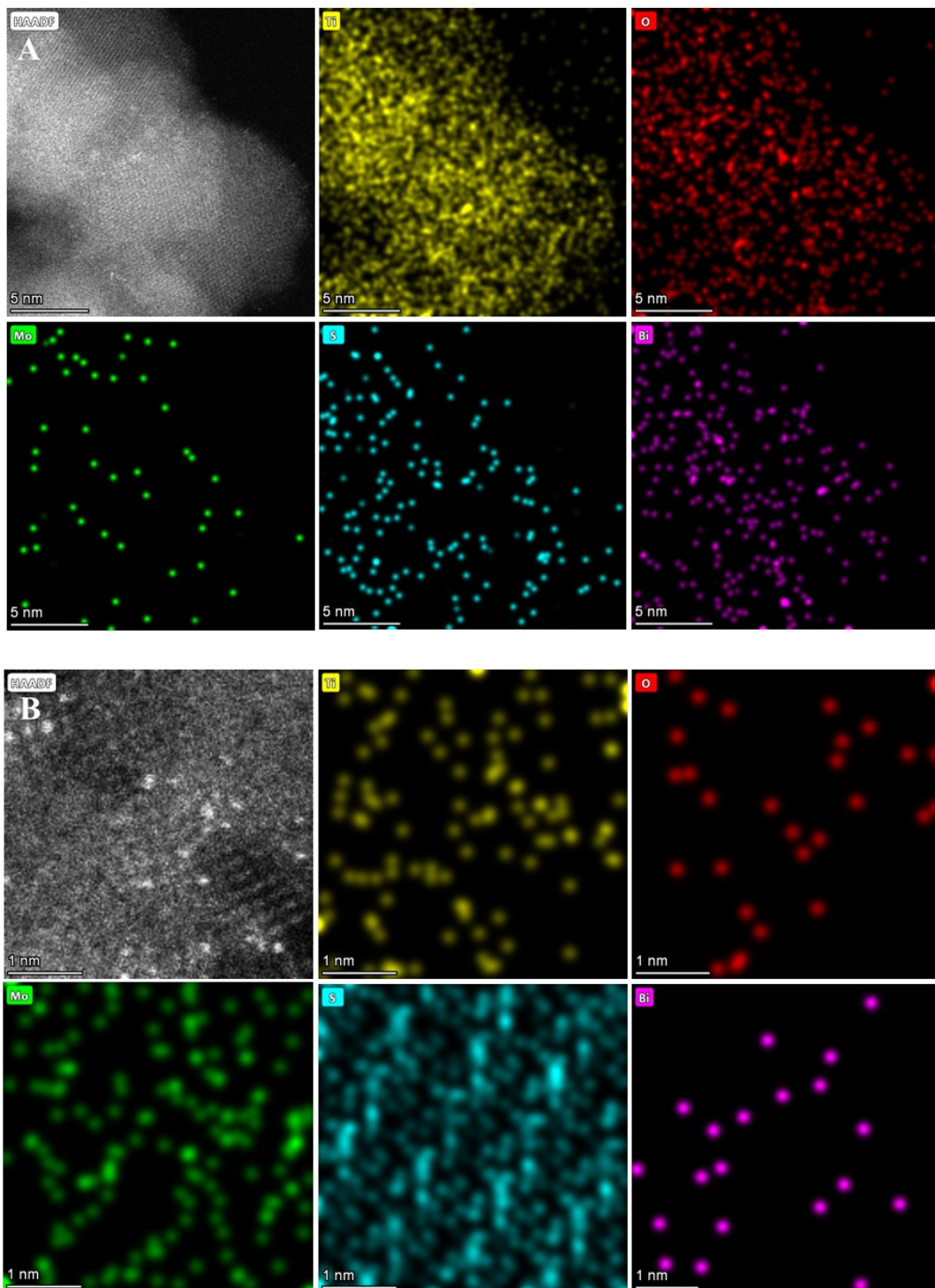
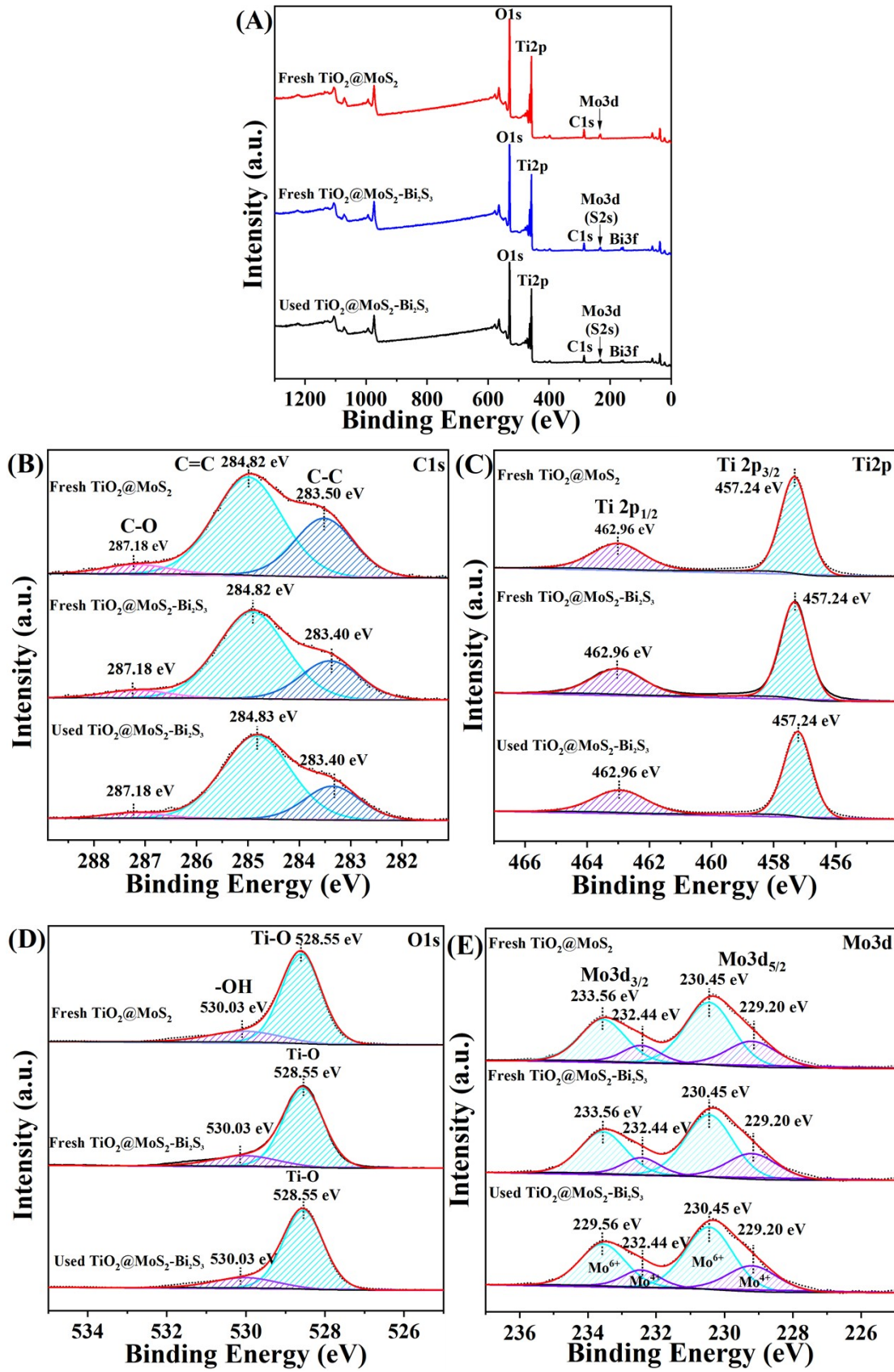


Fig. S3 High-angle annular dark-field scanning transmission electron microscopy (HAADF-STEM) with energy dispersive X-ray spectra of TiO_2 @ MoS_2 / Bi_2S_3



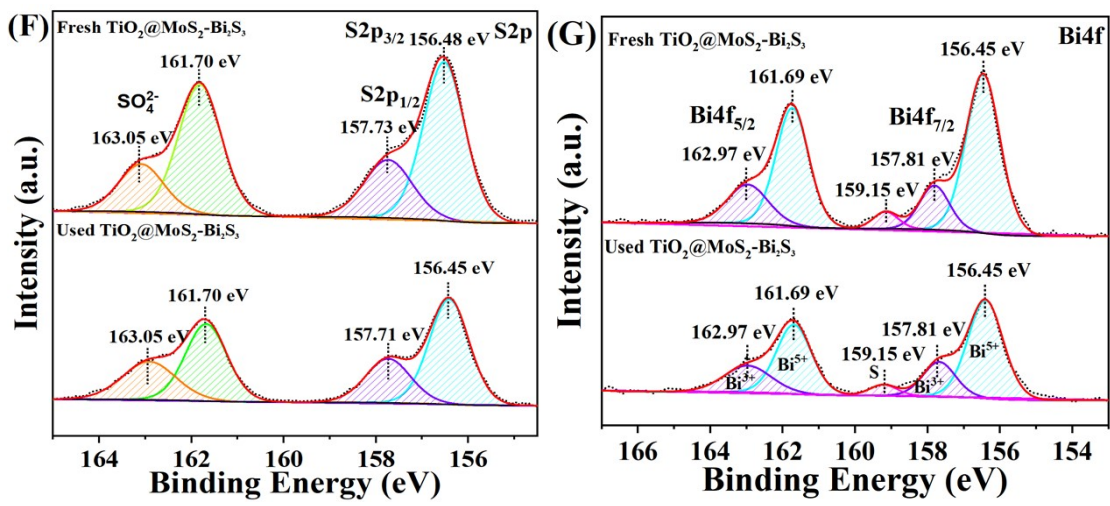


Fig. S4 XPS peak position spectra of $\text{TiO}_2@\text{MoS}_2$ -125, $\text{TiO}_2@\text{MoS}_2/\text{Bi}_2\text{S}_3$ -7 and the used $\text{TiO}_2@\text{MoS}_2/\text{Bi}_2\text{S}_3$ -7 samples: (A) global energy survey, (B) C1s, (C) Ti2p, (D) O1s, (E) Mo3d, (F) S2p and (G) Bi4f.

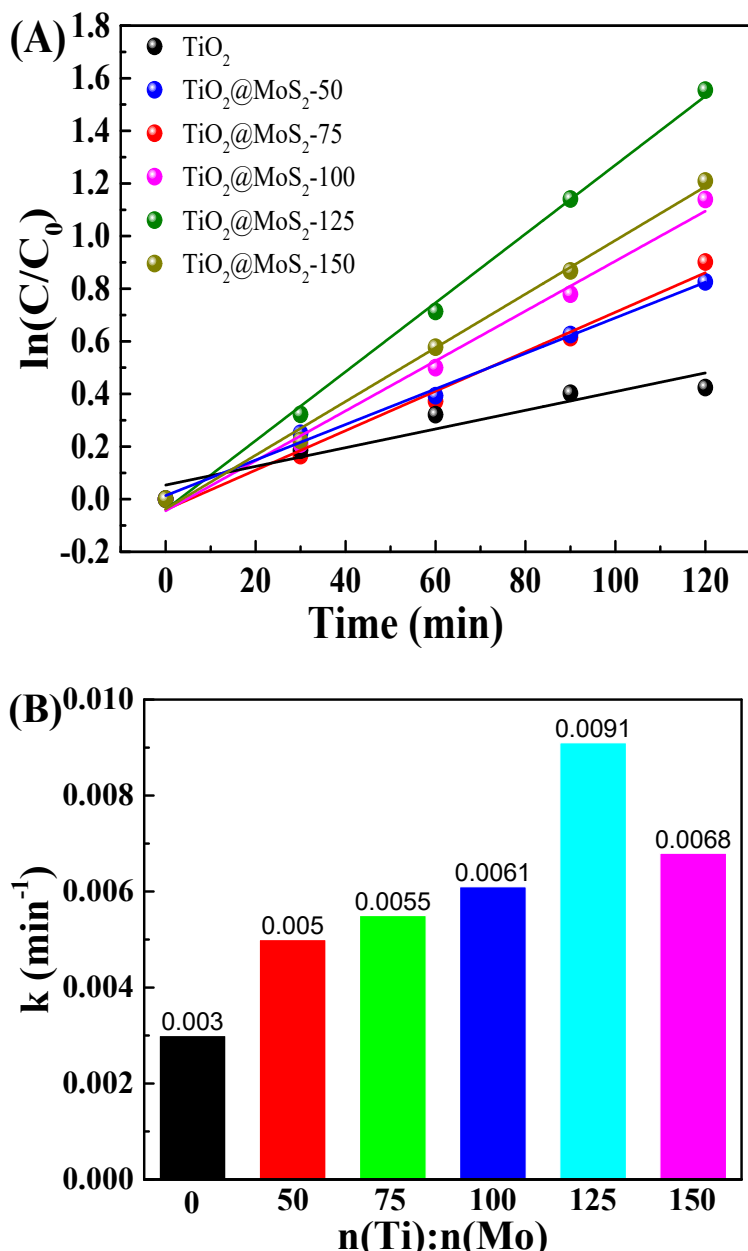


Fig. S5 (A) $\ln(C/C_0)$ vs reaction time and (B) rate constant of $\text{TiO}_2@\text{MoS}_2$ composite with different molar ratios curve and TiO_2

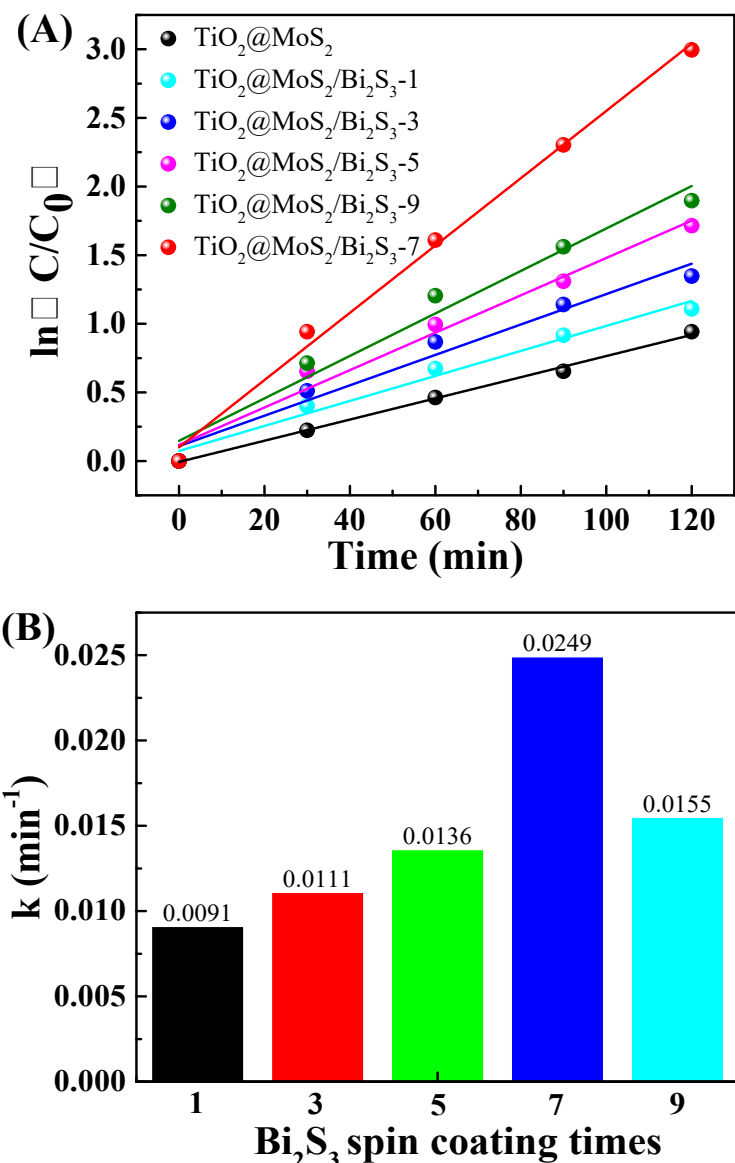


Fig. S6 (A) $\ln(C/C_0)$ vs reaction time and (B) rate constant of $\text{TiO}_2@\text{MoS}_2/\text{Bi}_2\text{S}_3$ composite with different Bi_2S_3 spin coating times

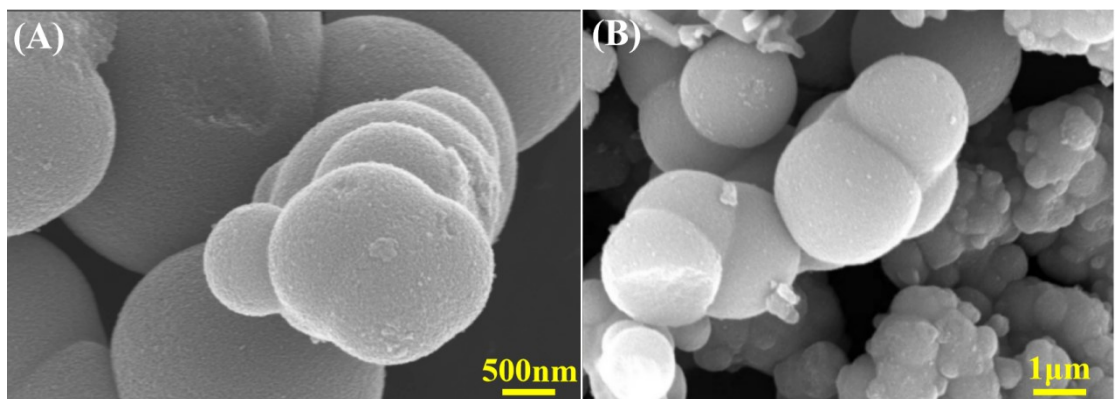


Fig. S7 SEM of recycling $\text{TiO}_2@\text{MoS}_2/\text{Bi}_2\text{S}_3$ -7 composites for five runs

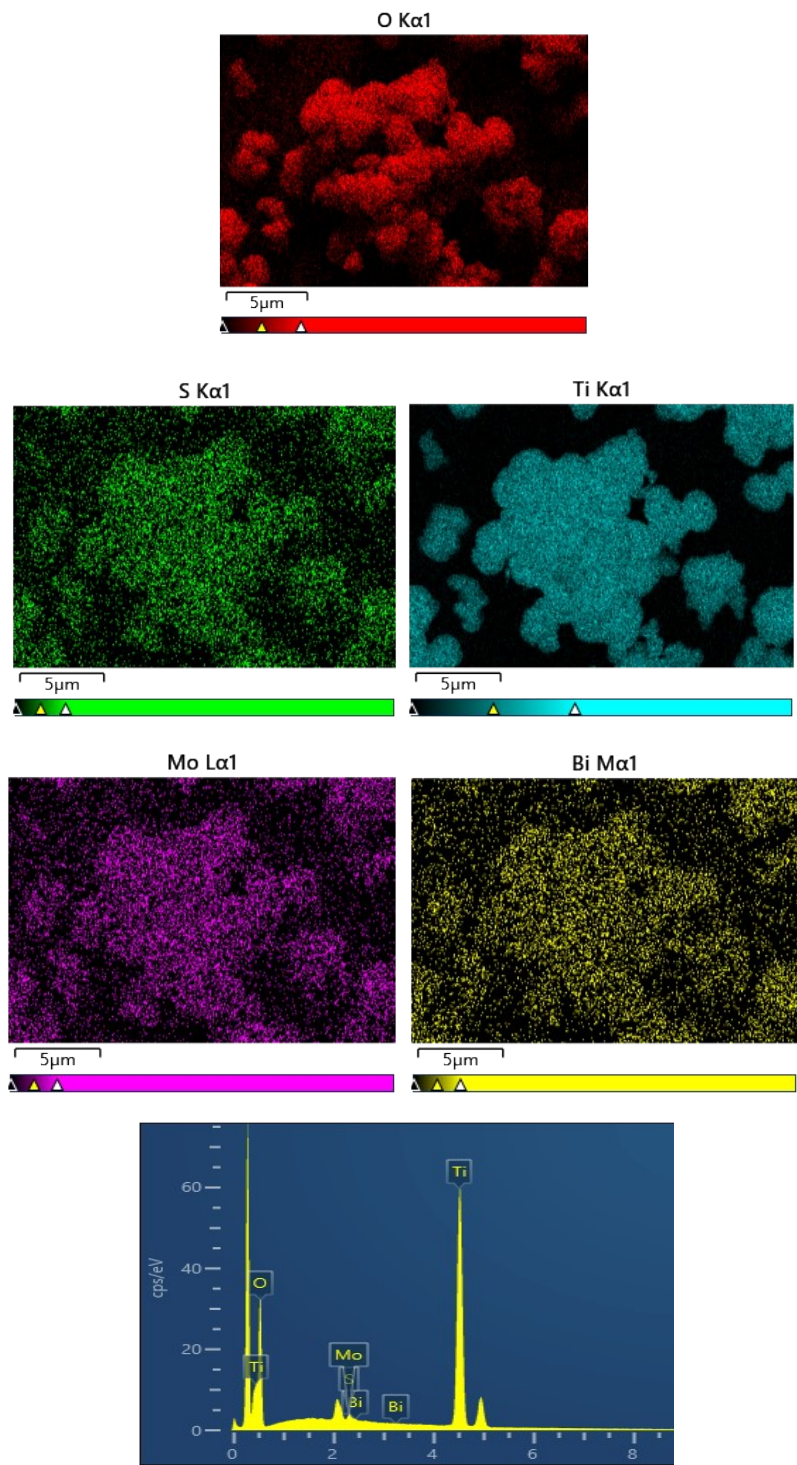


Fig. S8 EDS mapping of recycling $\text{TiO}_2@\text{MoS}_2/\text{Bi}_2\text{S}_3$ -7 composites and the corresponding EDS spectrum for 5th used $\text{TiO}_2@\text{MoS}_2/\text{Bi}_2\text{S}_3$ -7

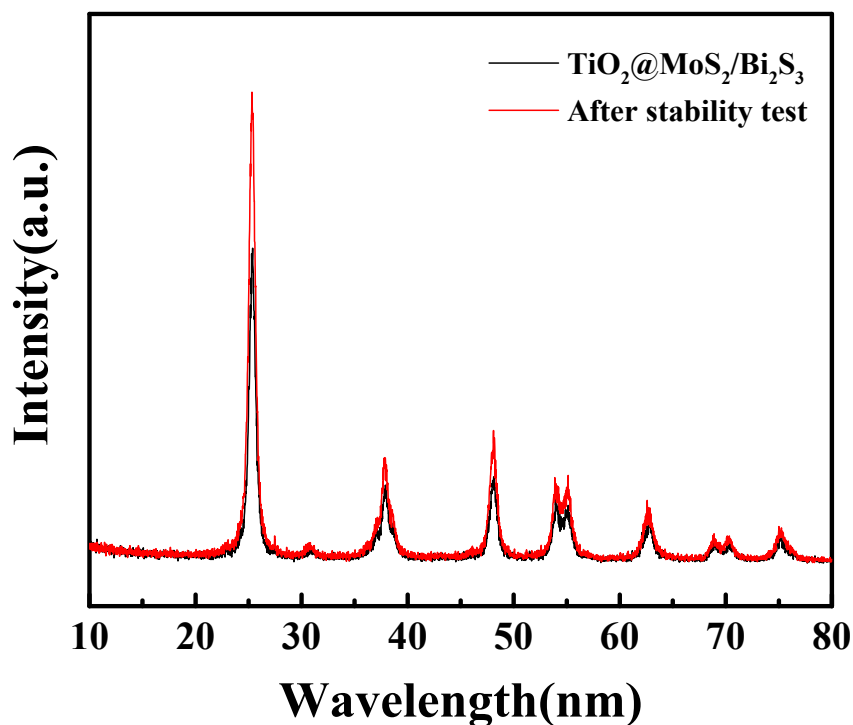


Fig. S9 XRD pattern of recycling $\text{TiO}_2@\text{MoS}_2/\text{Bi}_2\text{S}_3$ -7 compared with standard PDF card after stability test

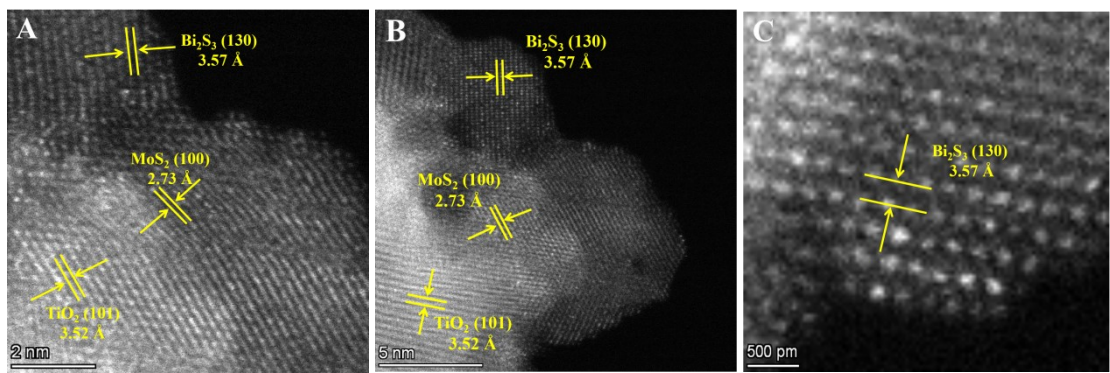


Fig. S10 High-angle annular dark-field scanning transmission electron microscopy (HAADF-STEM) of recycling $\text{TiO}_2@\text{MoS}_2/\text{Bi}_2\text{S}_3$

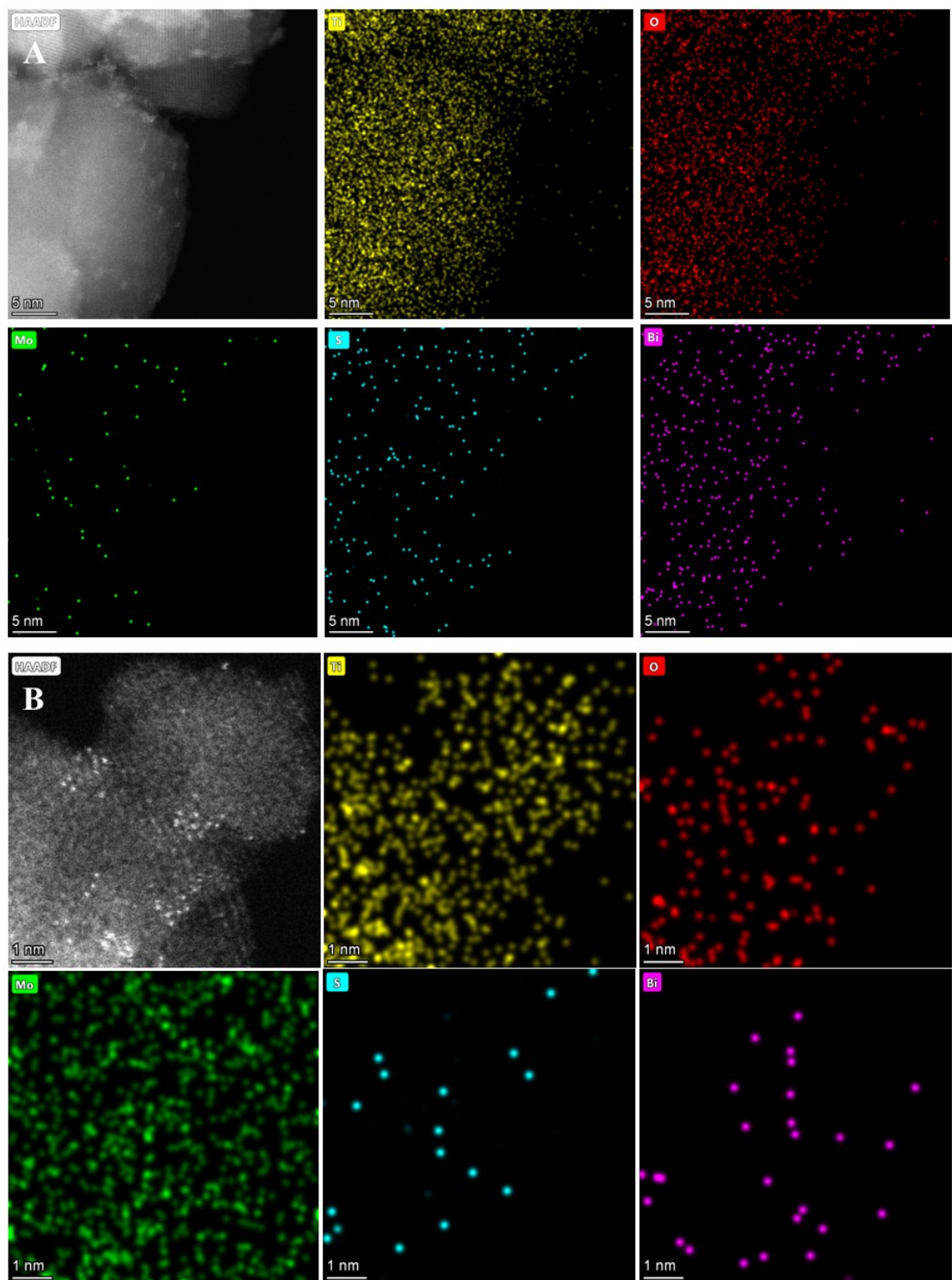


Fig. S11 High-angle annular dark-field scanning transmission electron microscopy (HAADF-STEM) with energy dispersive X-ray spectra of recycling $\text{TiO}_2@\text{MoS}_2/\text{Bi}_2\text{S}_3$

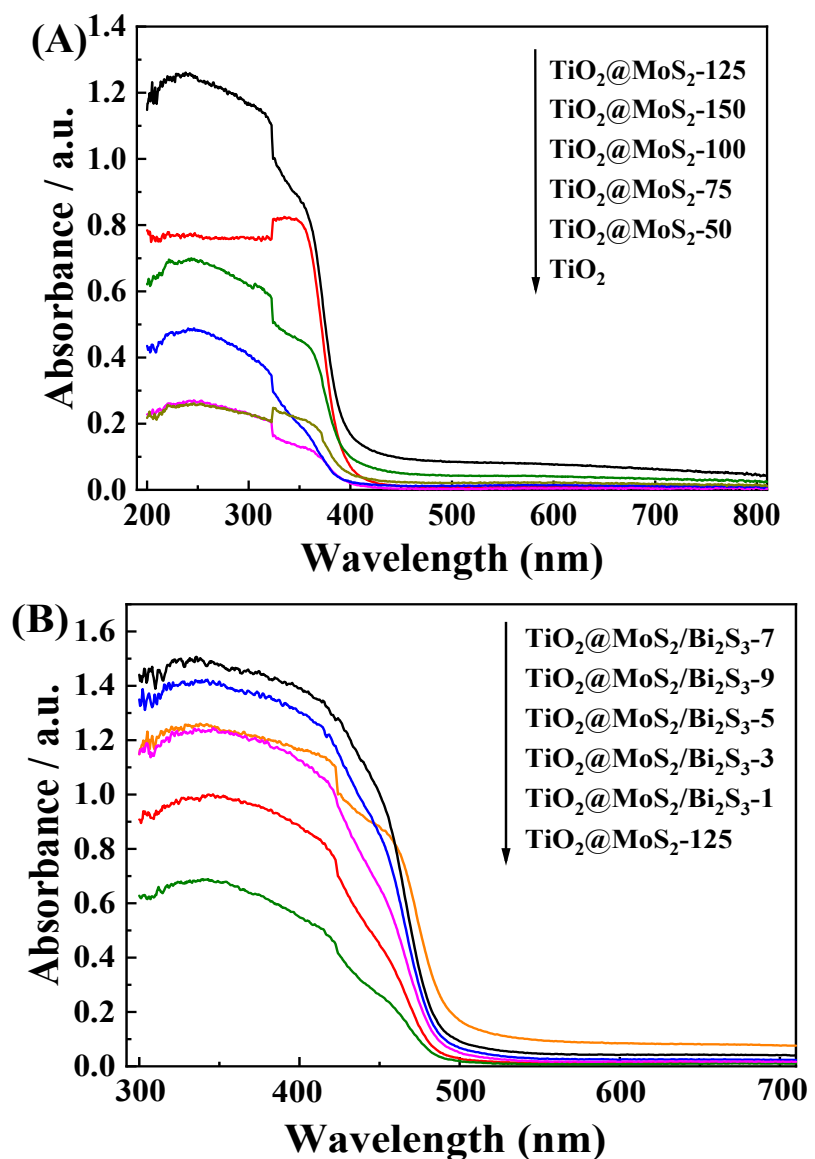


Fig. S12 UV-vis absorption spectra of (A) $\text{TiO}_2@\text{MoS}_2$ with different molar ratios and (B) $\text{TiO}_2@\text{MoS}_2/\text{Bi}_2\text{S}_3$ with different spin coating times

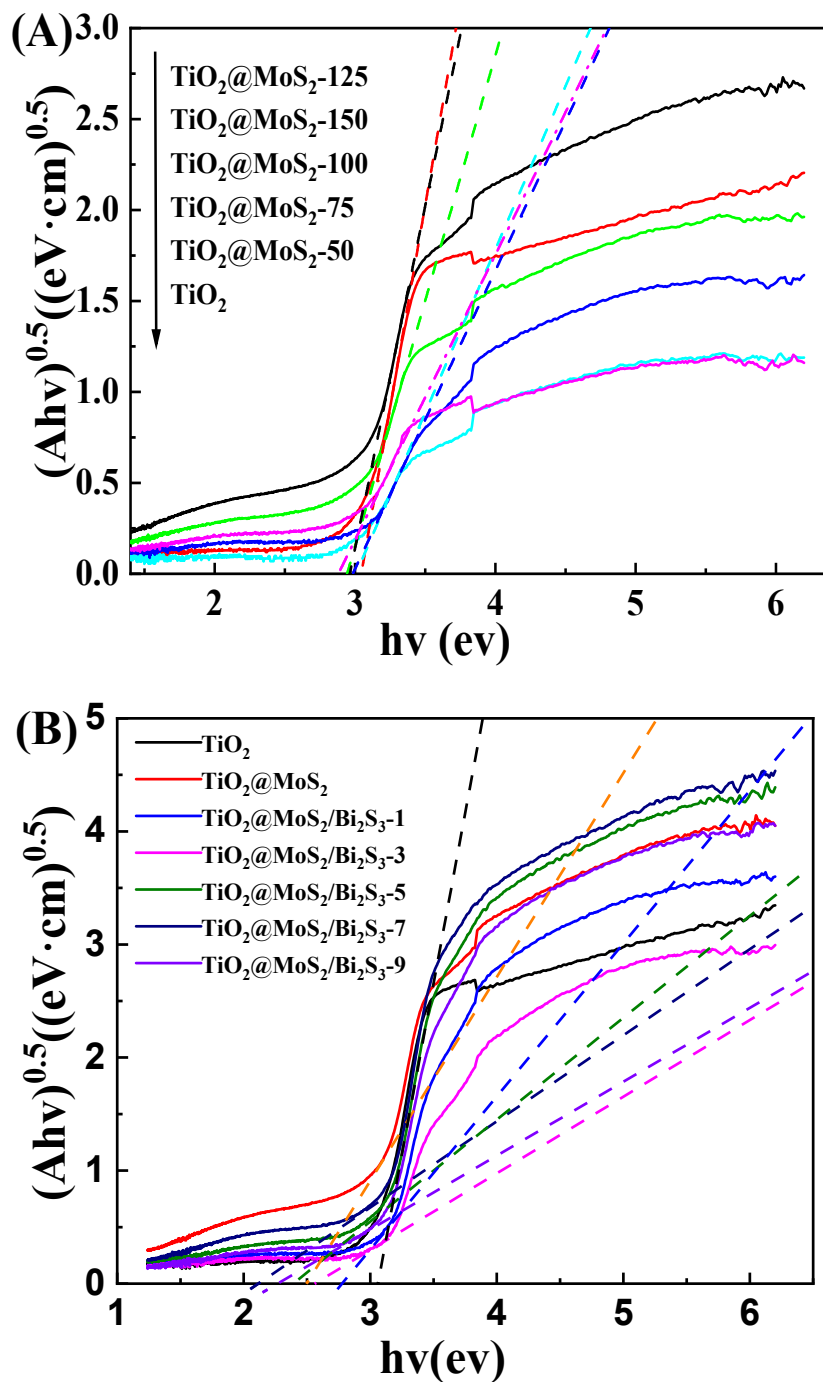


Fig. S13 Kubelka– Munk function VS the energy of incident light plots of (A) $\text{TiO}_2@\text{MoS}_2$ with different molar ratios and (B) $\text{TiO}_2@\text{MoS}_2/\text{Bi}_2\text{S}_3$ with different spin coating times

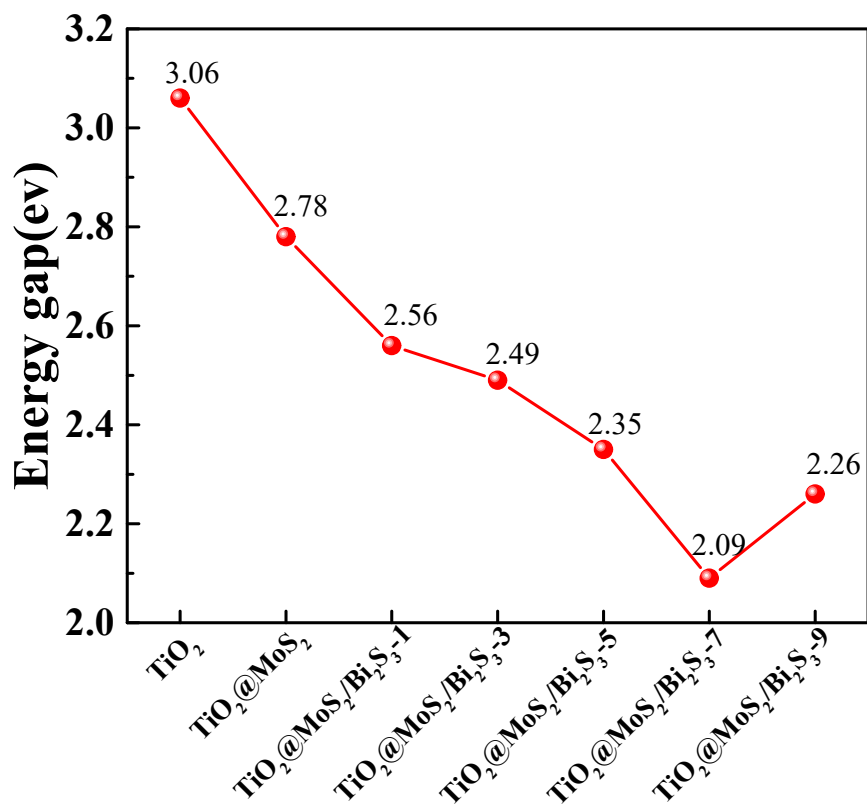


Fig. S14 Energy band gap of TiO_2 , $\text{TiO}_2@\text{MoS}_2$ and $\text{TiO}_2@\text{MoS}_2/\text{Bi}_2\text{S}_3$

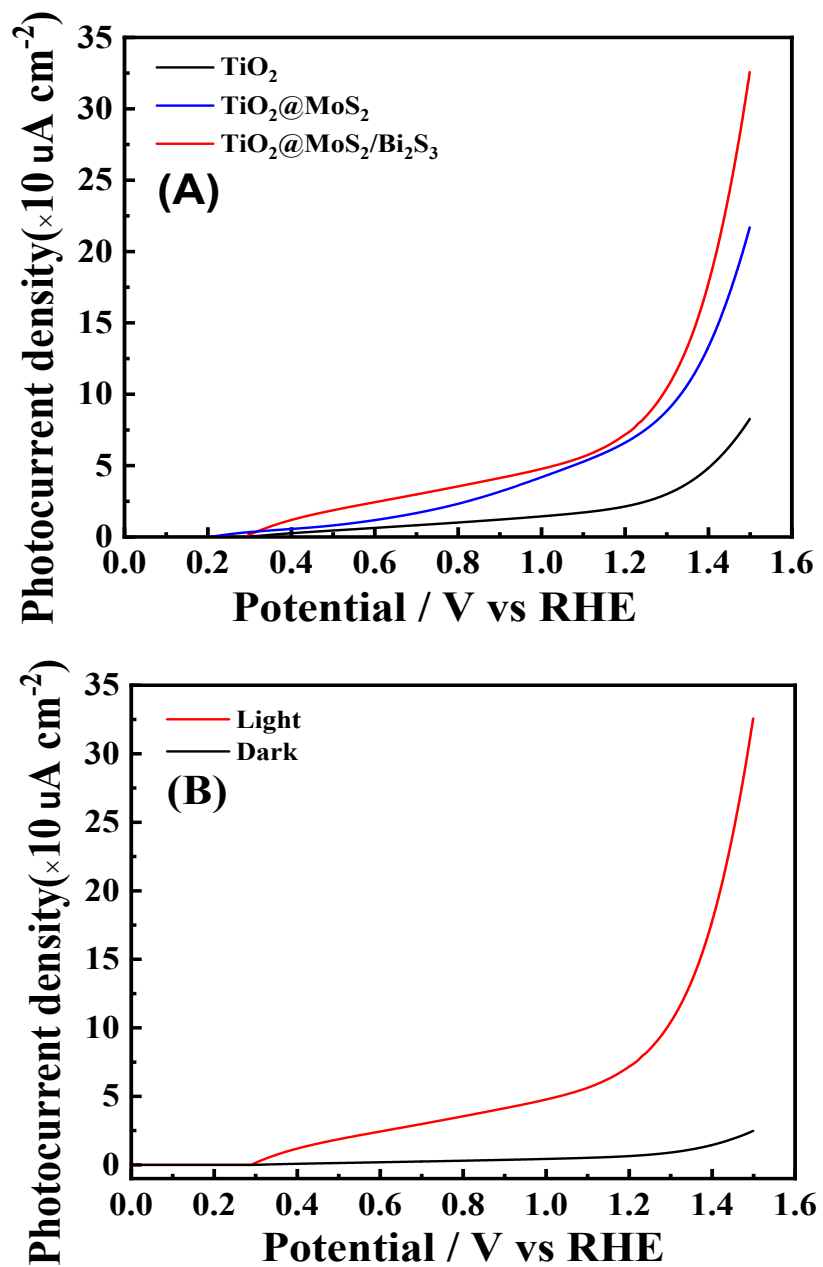


Fig. S15 (A) Linear Sweep Voltammetric (LSV) curves of TiO₂, TiO₂@MoS₂ and TiO₂@MoS₂/Bi₂S₃ under visible-light illumination, and (B) LSV curves of TiO₂@MoS₂/Bi₂S₃ under dark and visible-light illumination.

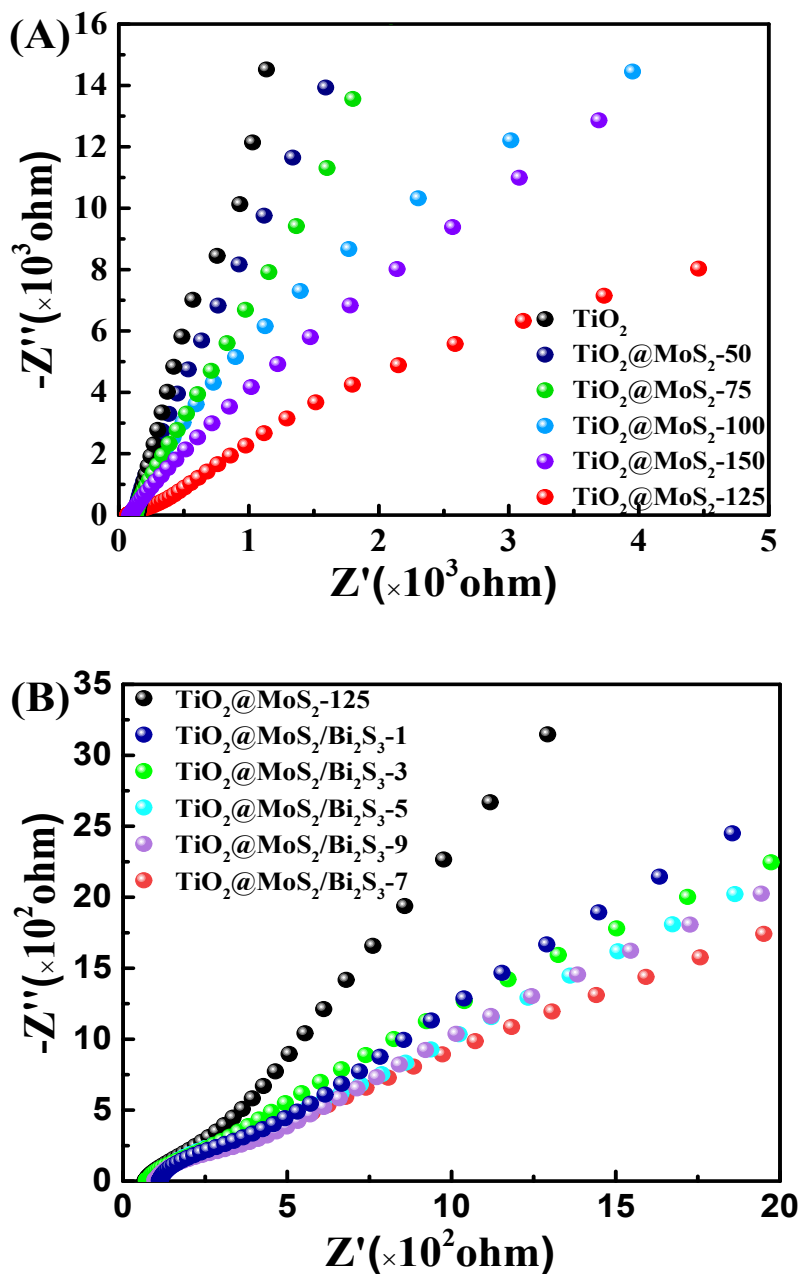


Fig. S16 Electrochemical Impedance spectroscopy (EIS) of (A) $\text{TiO}_2 @ \text{MoS}_2$ with different Mo doping proportions and (B) $\text{TiO}_2 @ \text{MoS}_2/\text{Bi}_2\text{S}_3$ with various Bi_2S_3 spin coating times at applied potential of 0.5 V

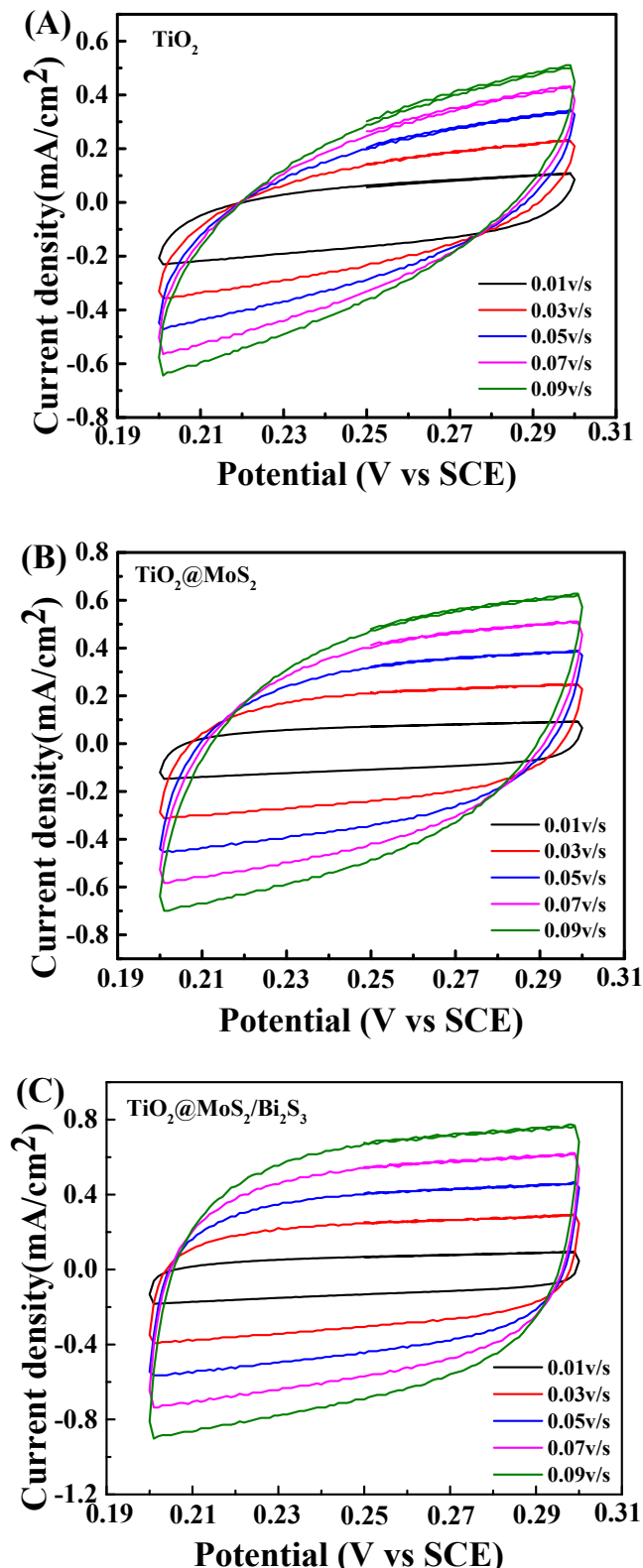


Fig. S17 Cyclic Voltammogram (CV) for (A) TiO_2 , (B) $\text{TiO}_2@\text{MoS}_2$ (C) and $\text{TiO}_2@\text{MoS}_2/\text{Bi}_2\text{S}_3$ in the region of $0.20 \sim 0.30$ V vs. RHE with various scans

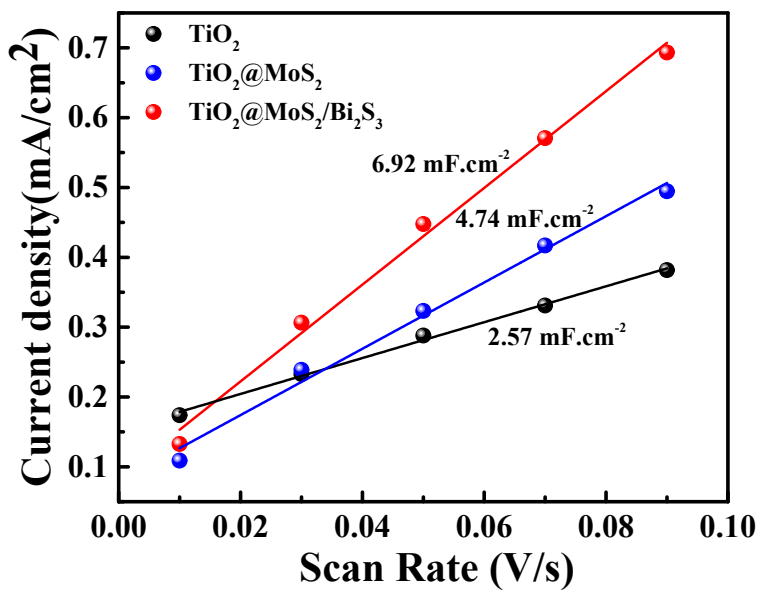


Fig. S18 Current density differences plotted against scan rates of TiO_2 , $\text{TiO}_2@\text{MoS}_2$ and $\text{TiO}_2@\text{MoS}_2/\text{Bi}_2\text{S}_3$

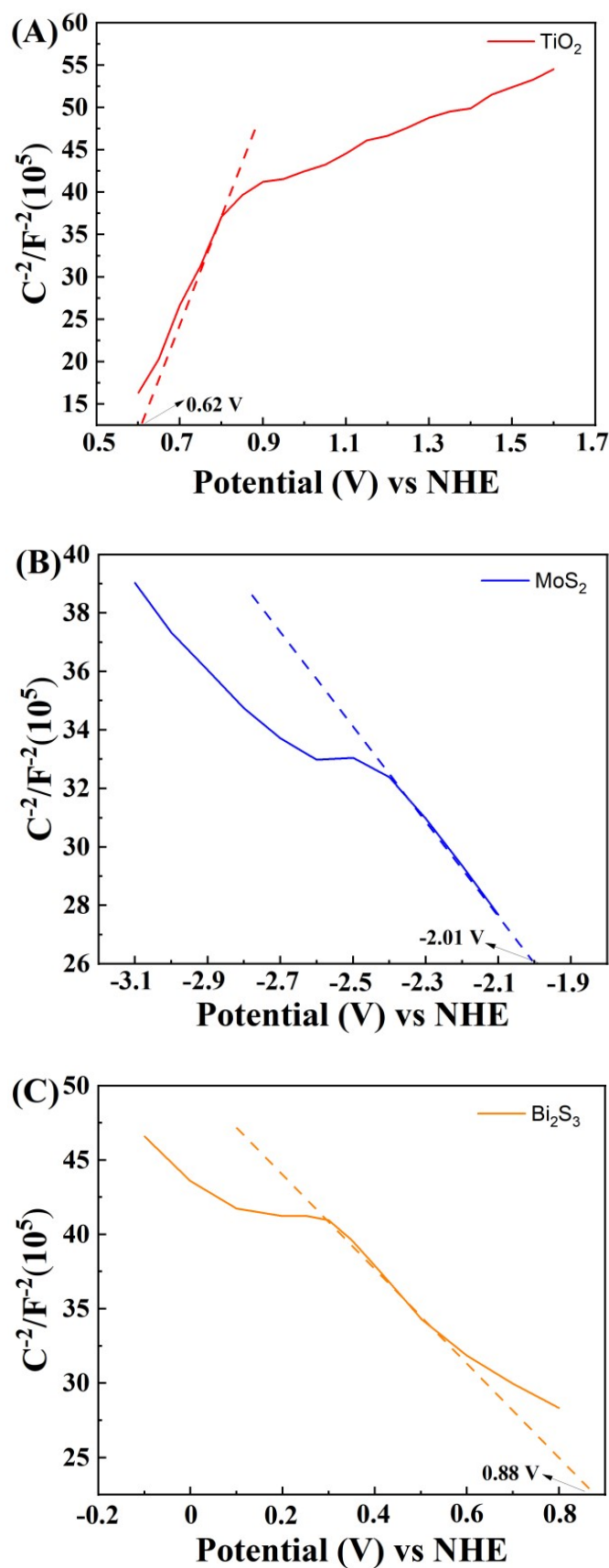


Fig. S19 Mott–Schottky (M–S) plots of (A) TiO_2 , (B) MoS_2 and (C) Bi_2S_3 separately

Quantitation experiments of •OH and O₂^{•-}

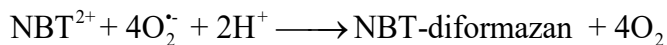
The generation concentrations of •OH and O₂^{•-} were measured through utilizing coumarin and nitrotetrazolium blue chloride (NBT). The •OH can react with coumarin to form 7-hydroxycoumarin (7-HOC), thus the production concentration of •OH could be estimated based on produced concentration of 7-hydroxycoumarin (7-HOC) due to linearly relationship between •OH concentration and rate of 7-HOC of production. Thus, steady-state concentration of •OH ([•OH]_{ss}) could be calculated through the following equation:

$$\text{Generation of } \cdot\text{OH} = 0.286 \times k_{\cdot\text{OH},\text{coumarin}} \times [\text{coumarin}]_0 \times [\text{OH}]_{ss}$$

$$\text{Where } k_{\cdot\text{OH},\text{coumarin}} = 6.4 \times 10^9 \text{ M}^{-1}\text{s}^{-1}$$

[coumarin]₀ indicates the initial concentration of coumarin. However, only 6.1% of generated •OH could be detected by this method due to the yield of 7-HOC produced by the •OH reaction. Therefore, the generation of •OH was divided by 6.1% in the calculation.

In addition, consuming amount of NBT could reflect O₂^{•-} generation amount because NBT was easily reduced to insoluble blue formaldehyde, thus was acted as molecular probe for determining O₂^{•-} amount. The steady-state concentration of O₂^{•-} ([O₂^{•-}]_{ss}) could be calculated through the following equation:



$$\text{Generation of } \text{O}_2^{\bullet-} = k_{\text{O}_2^{\bullet-},\text{NBT}} \times [\text{NBT}]_0 \times [\text{O}_2^{\bullet-}]_{ss}$$

Where $k_{\text{O}_2^{\bullet-},\text{NBT}} = 6.0 \times 10^4 \text{ M}^{-1}\text{s}^{-1}$, [NBT]₀ is the initial concentration of NBT.

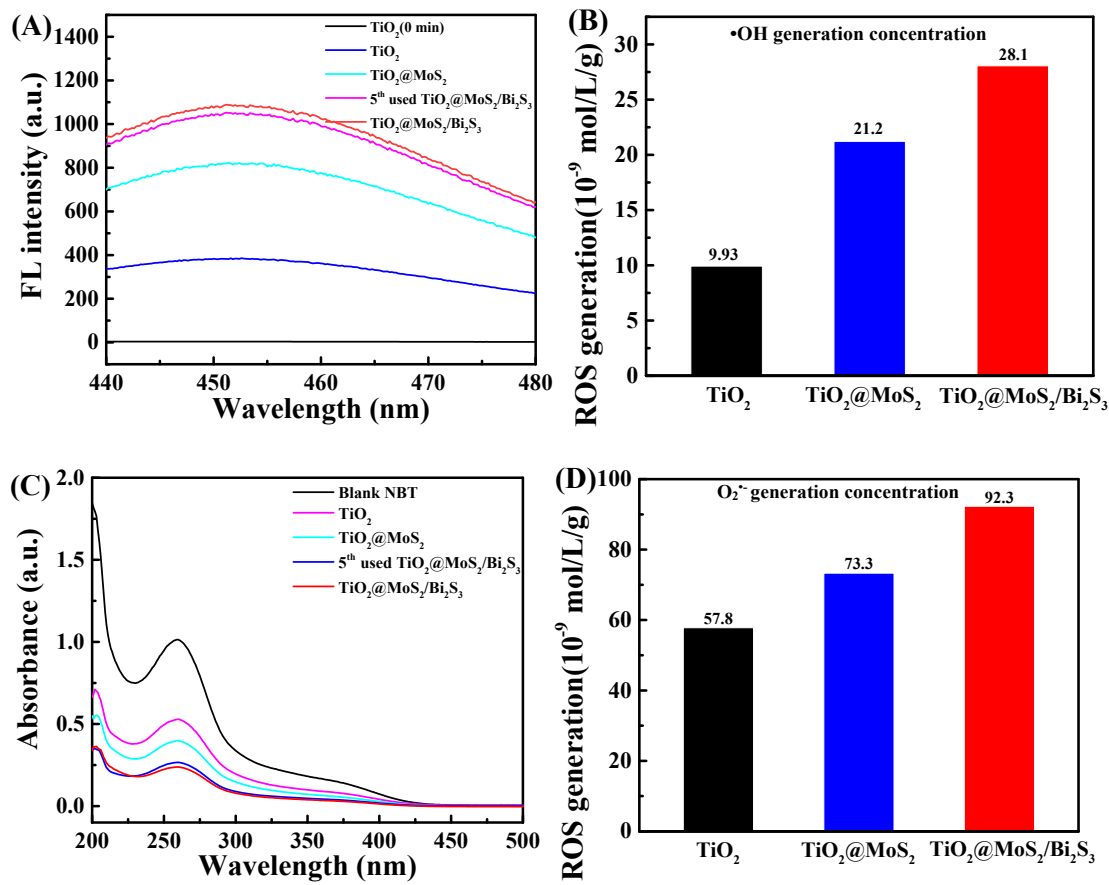


Fig. S20 (A) Fluorescence spectra of 7-hydroxycoumarin (7-HOC) in 0.1 mM coumarin solution and (B) •OH generation amount in the presence of various as-synthesized samples after 10 min visible-light illumination. (C) UV-Vis absorption spectra of NBT (2.5×10⁻² mM) and (D) O₂^{•-} generation amount on different as-synthesized samples after 10 min visible-light illumination

Reference:

- [S1] G. Kresse, J. Furthmüller, *Comp. Mater. Sci.* **1996**, *6*, 15.
- [S2] P.E. Blochl, O. Jepsen, O.K. Andersen, *Phys. Rev. B Condens. Matter* **1994**, *49*, 16223.
- [S3] J.P. Perdew, J.A. Chevary, S.H. Vosko, K.A. Jackson, M.R. Pederson, D.J. Singh, C. Fiolhais, *Phys. Rev. B Condens. Matter* **1993**, *48*, 4978.